The Hubble Sequence in groups: The birth of the early-type galaxies

Feldmann, R ; Carollo, C M ; Mayer, L

Abstract: The physical mechanisms and timescales that determine the morphological signatures and the quenching of star formation of typical (L*) elliptical galaxies are not well understood. To address this issue, we have simulated the formation of a group of galaxies with sufficient resolution to track the evolution of gas and stars inside about a dozen galaxy group members over cosmic history. Galaxy groups, which harbor many elliptical galaxies in the universe, are a particularly promising environment to investigate morphological transformation and star formation quenching, due to their high galaxy density, their relatively low velocity dispersion, and the presence of a hot intragroup medium. Our simulation reproduces galaxies with different Hubble morphologies and, consequently, enables us to study when and where the morphological transformation of galaxies takes place. The simulation does not include feedback from active galactic nuclei showing that it is not an essential ingredient for producing quiescent, red elliptical galaxies in galaxy groups. Ellipticals form, as suspected, through galaxy mergers. In contrast with what has often been speculated, however, these mergers occur at $z > 1$, before the merging progenitors enter the virial radius of the group and before the group is fully assembled. The simulation also shows that quenching of star formation in the still star-forming elliptical galaxies lags behind their morphological transformation, but, once started, takes less than a billion years to complete. As long envisaged the star formation quenching happens as the galaxies approach and enter the finally assembled group, due to quenching of gas accretion and (to a lesser degree) stripping. A similar sort is followed by unmerged, disk galaxies, which, as they join the group, are turned into the red-and-dead disks that abound in these environments.

DOI: https://doi.org/10.1088/0004-637X/736/2/88

Transformations in the Fall: The Birth of the Early-Type Galaxies

R. Feldmann[1,2], C. M. Carollo[1] & L. Mayer[3]

[1]*Department of Physics, ETH Zurich, 8093 Zurich, Switzerland*
[2]*Current address: Center for Particle Astrophysics, Fermi National Accelerator Laboratory, Batavia, IL 60510, USA; feldmann@fnal.gov*
[3]*Institute of Theoretical Physics, University of Zurich, 8057 Zurich, Switzerland*

Massive member galaxies of galaxy groups at redshift z=0 are mostly quenched systems with either a disk or an elliptical morphology[1]. Observations indicate that, to a large extent, this results from environmental forcing over the past eight billion years since redshift $z \sim 1$[2]. Many physical processes may be responsible for making elliptical morphologies and quenching star formation: major and minor merging, ram pressure stripping, accretion shocks, and removal of hot gas are among those that have been suggested as possible mechanisms[3–8]. Which of the many mechanisms are mainly responsible, and the epochs and timescales at/on which they operate, however, have not been yet identified. The challenge is to connect the large-scale, cosmological formation of the group, which affects the global evolution of group members, to the galactic sub-kpc scale, where star formation and stellar feedback dominate the physics of the gas and the galaxy morphology[9,10]. Here we report a simulation of the formation of a group of galaxies with sufficient resolution to track the evolution of gas and stars inside about a dozen galaxy group members over cosmic history. Ellipticals form, as suspected, through galaxy mergers. In contrast with what has often been speculated[11], however, these mergers occur at $z > 1$, before the merging progenitors enter the virial radius of the group and before the group is fully assembled. Quenching of star formation in the still star-forming elliptical galaxies lags behind their morphological transformation, but, once started, is taking less than a billion years to complete. As long envisaged[3,6,12], the quenching happens as the galaxies precipitate into the finally assembled group and are stripped of their gas - both hot and cold, in a temporal sequence. A similar sort is followed by unmerged, disk galaxies, which, as they join the group, are turned into the red-and-dead disks that abound in these environments[13].

Recent work shows that, despite the stellar mass function of galaxies itself depends on environment[14], the relative roles of mass and environment in the formation of the Hubble sequence can be nonetheless disentangled in the observations[2]. Both numerical simulations of the galaxy population in a cosmological context and semi-analytical models of galaxy formation have however lacked so far the ability to describe at once the various environmental processes that can affect the baryonic component of galaxies, due to lack of resolution and the incomplete knowledge of the interplay between such processes. Therefore, despite the observational evidence that galaxy evolution is affected by the galactic environment, how this happens within the cold dark matter scenario for the formation of cosmic structure is highly debated today. This notwithstanding the results of detailed, small scale numerical models, abstracted from the large scale cosmological context, have repeatedly shown how mergers, tidal interactions, ram pressure stripping of the cold and hot gas phase as well as gas accretion from the surrounding intergalactic medium can change the morphology of individual galaxies, and alter their star formation rates and colors. Recent progress in the modeling of the formation of galaxies in the cosmological context has finally shown that realistic galaxies can be formed in the cold dark matter model once galaxies are resolved with $\sim 10^5$ baryonic particles and at a sub-kpc resolution[10,15], but this has only been achieved so far for individual galaxies in low density (field) environments. Therefore, key questions

remain when, and how, the disks are transformed into spheroids, star formation is quenched, and stellar mass is accreted in the massive galaxies that end up residing preferentially in the dense environments at $z = 0$.

Here we address these key questions with the help of a cosmological hydrodynamical simulation that follows the concurrent evolution of many galaxies before, during and after they join a relatively dense, group-sized virialized region with $R_{200} = 396$ kpc and $M_{200} = 1.1 \times 10^{13}\ M_{\odot}$ at $z \sim 0$. Our simulation is run with the parallel TreeSPH code GASOLINE[16]. The mass and force resolution (for SPH particles, $\sim 10^6\ M_{\odot}$ and 0.3 kpc, respectively) is comparable to state-of-the-art cosmological simulations of individual disk galaxies[10,17] and allows to accurately resolve the half-mass radii of the massive group members (~ 1 kpc). Besides following gravitational, hydrodynamical and optically thin radiative processes of matter in an expanding Universe directly, the simulation includes modeling of star formation, feedback from type Ia and type II supernovae, mass loss by stellar winds, and metal enrichment using parameters that were originally tuned to produce disk galaxies in galactic halos[10,18]. As we show below the same physical prescriptions produce, when used to simulate a relatively massive potential of a group of galaxies, $z = 0$ galaxies with a broad range of luminosities, sizes and kinematics, which are consistent with the properties of disk and elliptical galaxies in the local Universe.

The simulation was evolved down to redshift $z \sim 0.1$. At this epoch, thirteen well-resolved galaxies, with stellar masses $> 10^{10}\ M_{\odot}$, orbit in, or near, the galaxy group, whose stellar mass budget is dominated by an early-type galaxy at its center[19], see Fig. 1. The mass range of these satellite galaxies straddles across the transition mass of $\sim 3 \times 10^{10}\ M_{\odot}$ below (above) which most galaxies in the local universe have a disk (early-type) morphology. Indeed, Fig. 2 shows that, at $z = 0$, the simulated galaxies span a broad range in morphological properties, from very flat disks to almost spherical spheroids, as well as in rotational support ($v_{\rm rot}/\sigma_{\rm cen} \sim 0.4 - 1.3$), color ($B - I = 0.6 - 1.3$ mag), neutral hydrogen fraction ($f_{\rm gas} \sim 0 - 5\%$), and star formation rates (SFRs). Properties range from passively evolving galaxies to moderately star forming systems, with SFRs that are typical of similar mass $z = 0$ disks, i.e., $\sim 1\ M_{\odot}{\rm yr}^{-1}$.

Bulge to disk decompositions remain challenging even at the sub-kpc resolution of our simulation. However, based on standard morphological classification criteria that use global galactic properties such as the ratio of stream-to-dispersion velocities, and the index of single-component Sersic fits to the surface brightness profiles, we identify six group members as rotationally supported, disk galaxies ($v_{\rm rot}/\sigma_{\rm cen} \geq 1$, $n_{\rm Sersic} < 2.5$). These galaxies show a range of colors and star formation rates that range from those of normal star-forming spirals to those of passive spirals/S0 galaxies. Specifically, three of the disk galaxies have red colors ($B - I \sim 1.2 - 1.3$), contain no significant amount of neutral hydrogen ($< 1\%$), and have stopped forming stars (top right in Fig. 2). The three other disk galaxies, instead, have bluer colors ($B - I \sim 0.6 - 0.9$), significant neutral hydrogen fractions ($\gtrsim 3\%$), and SFRs of order unity (top left in Fig. 2). The remaining seven satellites have properties that are typical of early-type (hereafter 'elliptical') galaxies, i.e., $n_{\rm Sersic} \geq 2.5$ and $v_{\rm rot}/\sigma_{\rm cen} < 1$.

At $z \gtrsim 1$, the most massive progenitors of the $z = 0$ group satellite galaxies are blue ($B - I < 1$), strongly star forming (specific SFR $> t_{\rm H}^{-1}$), gas-rich ($f_{\rm gas} \sim 20\%$), rotationally-supported ($v_{\rm rot}/\sigma_{\rm cen} \geq 1$) galaxies (Supplementary Information). In the simulation we can trace when, and how, the progenitor disks of the passively-evolving spheroids and 'gas-starved' disks, exhausted and/or expelled their fuel for star formation, and when and how they transformed their morphologies (in those cases they did).

Major galaxy mergers are in most cases responsible for the morphological transformation of disk galaxies

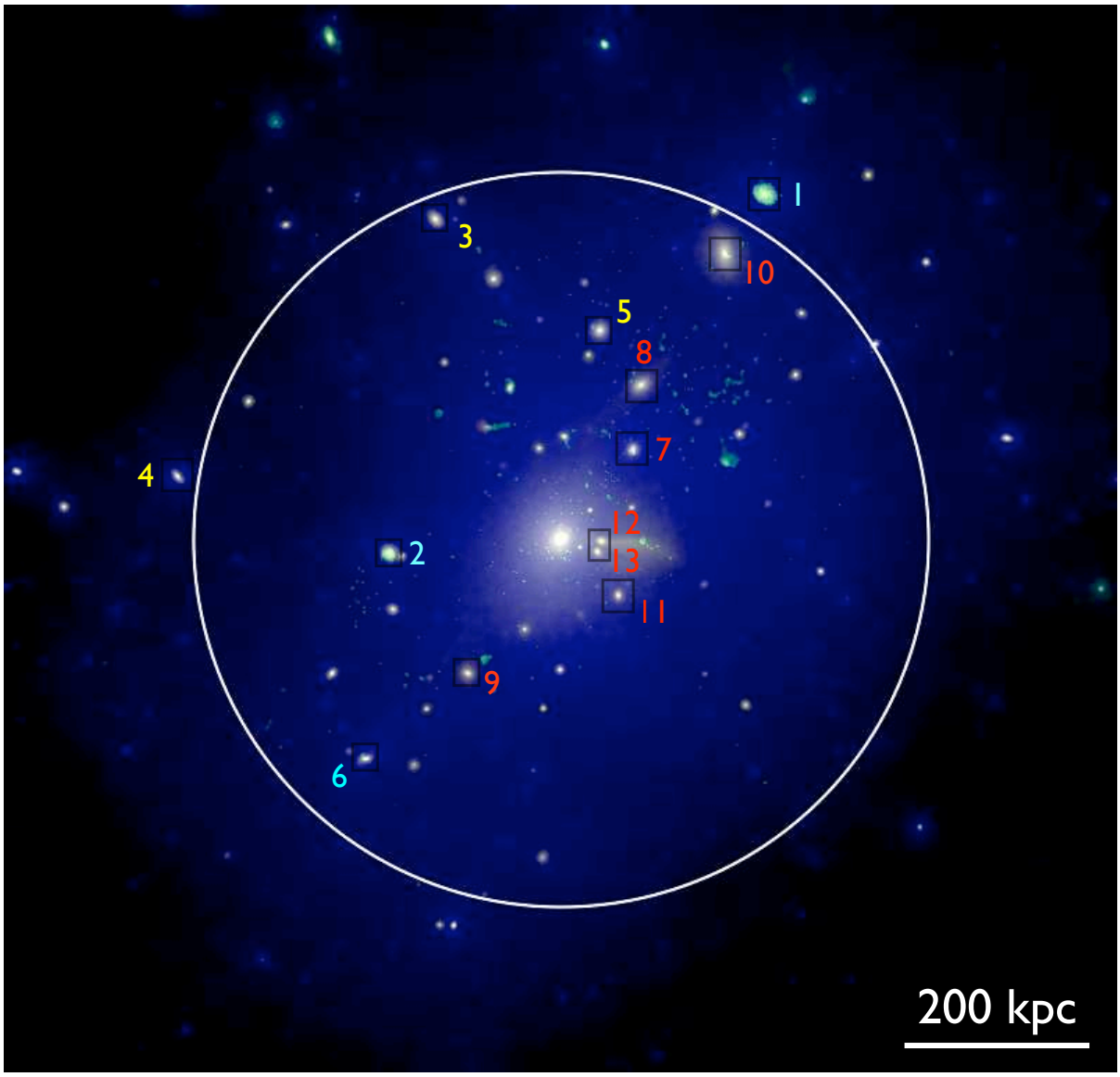

Figure 1: **The simulated group at** $z = 0.13$**.** A massive central galaxy is surrounded by a large number of massive satellite galaxies. The image is 1.2 Mpc $\times$ 1.2 Mpc across and shows the projected mass densities of dark matter (blue; from 1.45 to 1450 $M_\odot$ pc^{-2}), neutral hydrogen (green) and stellar matter (yellow; both from 0.36 to 365 $M_\odot$ pc^{-2}). The white circle indicates the virial radius $R_{200} = 396$ kpc of the group. The properties of the satellites with a stellar mass $> 10^{10}$ $M_\odot$ (numbered) are shown in Fig. 2. The galaxies are either entering the group for the first time (e.g., galaxy #1), or orbit within the virial radius of the group, or already crossed the group and are now at an apocenter (e.g. galaxy #4).

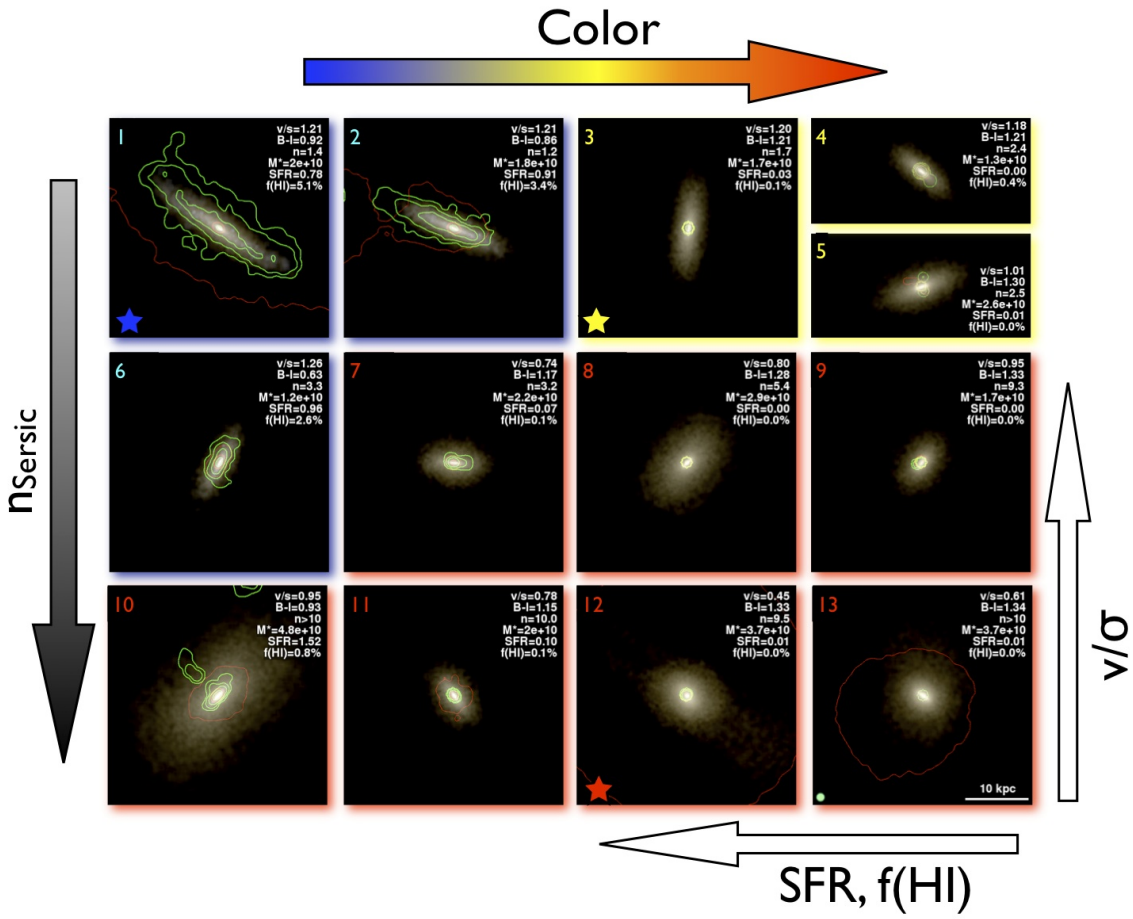

Figure 2: **Massive ($M > 10^{10} M_{\odot}$) galaxies orbiting within the group at $z \sim 0.1$.** Each composite image shows an edge-on view, i.e. a view along the intermediate axis of the reduced moment-of-inertia tensor of the stellar component within 10 kpc, of a satellite galaxy. The galaxies are arranged w.r.t. their colors, Sersic index, rotational support, star formation rate and gas fraction. Fundamental galaxy properties are shown at the top right of each panel (SFR in $M_{\odot}$ yr^{-1}). Galaxies #1, #2 and #6 are classified as normal disk galaxies, #3, #4, #5 as gas-poor disks and #7 − #13 as elliptical galaxies. A representative of each class is marked with a colored star. (Red star) This galaxy has a red color, hosts virtually no neutral gas, is almost spherical (sphericity of the stellar component $c/a = 0.77$), has a steep surface mass profile and its kinematics is dominated by velocity dispersion. (Yellow star) The galaxy is a red gas-poor, rotating disk galaxy ($c/a = 0.38$) with an I-band exponential scale length $a_I = 1.4$ kpc. (Blue star) This galaxy hosts $\sim 10^9$ $M_{\odot}$ of HI, has a bluer $B - I$ color, and harbors a rotating stellar disk ($c/a = 0.36$) with $a_I = 2.3$ kpc. The RGB color channels of the images correspond to the surface brightness in the restframe Bessel B, R and I filterbands, respectively, and range from 16 mag arcsec^{-2} to 24.5 mag arcsec^{-2}. Green contour lines indicate the column densities of neutral hydrogen corresponding to 0.1, 1, 10, 100 $M_{\odot}$ pc^{-2}, while thin (thick) red contours correspond to column densities of 1 (10) $M_{\odot}$ pc^{-2} of bound hot ($T > 2.5 \times 10^5$ K) gas. The asymmetric gas contours in the two top left panels reveal the action of ram-pressure as the satellites move through the intra-group medium. The scale of all images is indicated in the bottom right panel. The green circle at the bottom-left corner of panel 13 has a radius of 2 gravitational softening lengths and indicates the resolution limit of the simulation.

into systems with an elliptical morphology. Remarkably, and rather unexpectedly, however, these transformations happen before galaxies accrete onto the massive potential of the group. They produce six out of the seven ellipticals that are present in the group by the present epoch. Therefore, while groups have always been considered as the natural site for major galaxy mergers given their low velocity dispersion, we find that elliptical galaxies in groups are the result of pre-processing at $z \gtrsim 1$, caused by interactions occurring when galaxies are still distinct objects embedded in their individual halos. The galaxies are also still gas-rich when they undergo such mergers, and they will lose their gas only later when they will fall into the virialized region of the group. Fig. 3 shows that the progenitors of $z \sim 0$ elliptical satellites all suffered from (moderately dissipative, $f_{\rm gas} \sim 10 - 20\%$) major ($> 1:6$) merger events (see also Fig. 4) over the $z \sim 1 - 2$ period. In contrast, the progenitors of $z = 0$ disk satellites have a rather quiet and uneventful history: none of them experiences a significant ($> 1:10$) stellar merger after redshift $z \sim 2$. These galaxies grow their stellar mass by in-situ star formation, which typically proceeds at a rate $\sim 1\ M_\odot\ {\rm yr}^{-1}$ at $z < 1$. The mergers that produce the elliptical morphologies naturally lead to a faster growth of stellar mass relative to in-situ star formation.

The group potential plays on the other hand a crucial role in removing the gas reservoir of all galaxies and truncating their star formation. As a result, the photometric evolution of ellipticals into the passively evolving early-type galaxy population observed at the present epoch lags behind by several Gyr the time at which their spheroidal morphology is established in the mergers at earlier epochs. Likewise, the transformation of normal star forming disks into gas-poor, 'starved' red disks appears to be mostly a consequence of their infall into group environment. Indeed, the three disk galaxies that are gas-poor and quiescent by $z = 0$ enter the group at earlier epochs than the three $z = 0$ star forming disks (respectively $z = 0.35, 0.49, 0.80$ and $z = 0.13, 0.19, 0.26$), and are exposed for longer periods to the physical processes that are most effective in the group environment. Such processes are, precisely, suppression of gas accretion as well as ram pressure stripping of both the hot and cold gas reservoir; in-situ star formation is responsible for consuming a substantial fraction of the residual gas. In detail, a galaxy that plunges into the depth of the group potential is first observed to stop accreting gas after the infall. Subsequently, a substantial amount of its hot halo gas is removed by ram-pressure stripping on its first orbit within the group, namely on a timescale of a Gyr or so, consistent with a 'starvation' picture[6,20], see Supplementary Information. Most of the cold gas ($\sim 90 \pm 10\%$) is then lost within the following ~ 1 Gyr, through star formation ($\sim 70\%$) as well as nearly instantaneous ram pressure stripping at pericenter passages. For galaxies falling into the final virialized group halo, the first pericenter passage is reached 0.4 ± 0.1 Gyr after infall into the group, i.e., the characteristic crossing time of the group.

In Fig. 4 we illustrate, as an example, how the transformation into a gas-poor, quiescent, red, velocity-dispersion supported elliptical galaxy takes place as a 'two-step' process, starting from gas-rich, star-forming, blue, rotating galaxies. First, at $z \sim 1.1$ and at ~ 1 Mpc distance from the group center, a gas-rich merger with a stellar mass ratio $\sim 1:2$ destroys the stellar disk of the more massive progenitor. The remnant relaxes in a few hundred Myr to an elliptical morphology, but its colors remain blue and it still hosts a substantial amount ($\sim 10^9\ M_\odot$) of HI within 20 kpc. During the merger the star formation rate is substantially enhanced[21]; at its peak, it is about a factor five higher than the average rate that the galaxy experiences throughout its history. Thereafter the HI reservoir and the SFR gradually decrease. After the first pericenter, the SFR and the HI content become negligible and the galaxy turns into a red, passively evolving ($\sim L^*$ in the Sloan Digital Sky Survey $z = 0.1$ redshifted r-filter[22]) elliptical, with a final $B - I = 1.34$.

We note that one of the seven $z = 0$ elliptical satellites does not undergo any substantial merger since

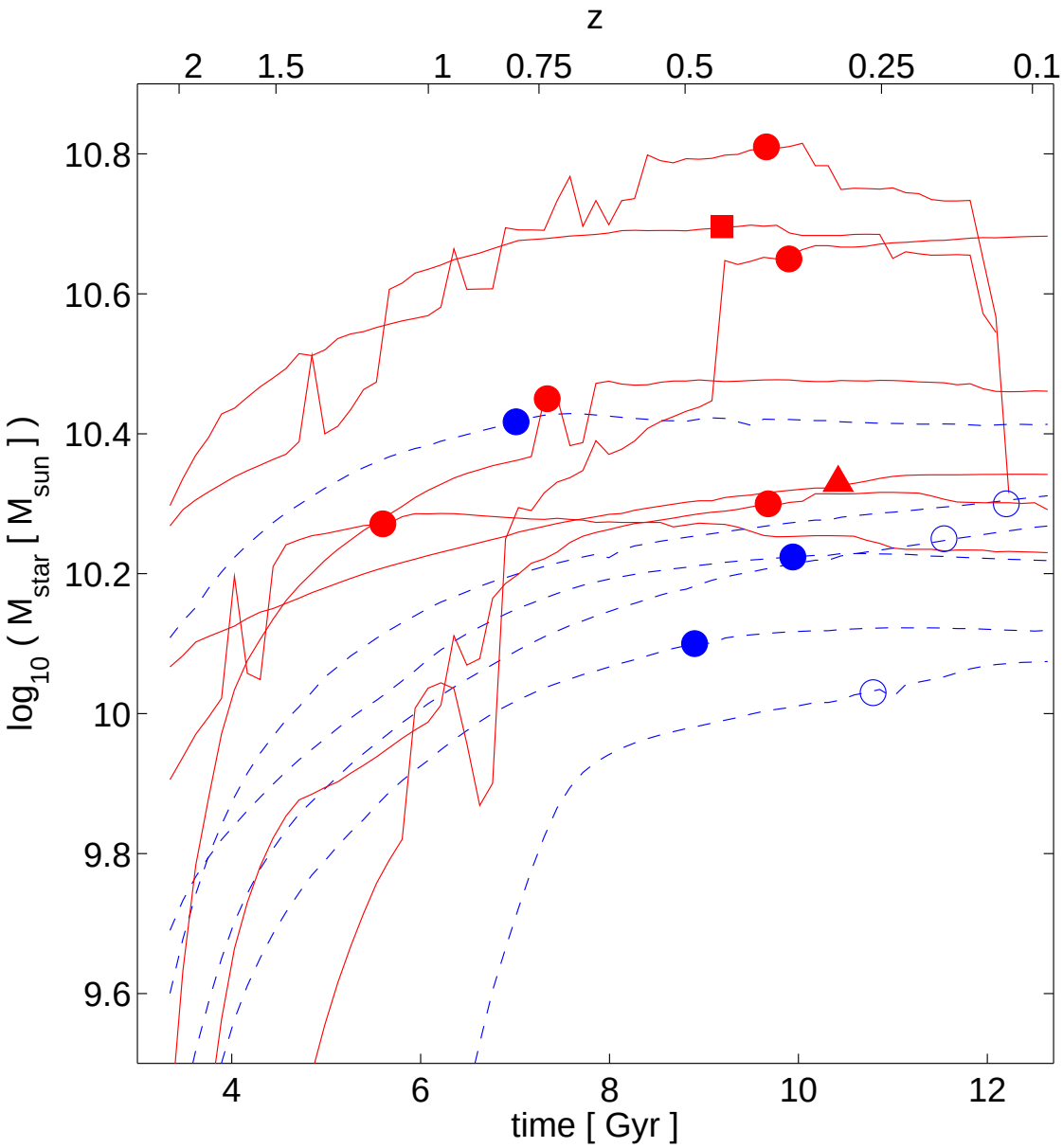

Figure 3: **Assembly histories since $z = 2$ of all $z \sim 0.1$ group members with a stellar mass above 10^{10} $M_{\odot}$.** Red solid (blue dashed) lines show the stellar mass of $z \sim 0.1$ elliptical (disk) satellites as function of time (bottom axis) and redshift (top axis). Filled (empty) symbols indicate the time when the progenitor of a $z \sim 0.1$ gas-poor (intermediate-gas) satellite enters the virial radius of the group. Sudden increases in stellar mass are caused by merger events, often before infall into the group, while close pericentric passages that lead to tidal stripping reveal themselves through a step-wise stellar mass loss occurring after their entrance in the group. The gas-poor disk satellites do not grow significant stellar mass after they enter the group, due to quenching of their star formation. One of the elliptical satellites does not show signs of significant merging since $z \sim 2.2$ (red triangle). This galaxy assembles most of its stellar mass early on, before such epoch, i.e., much earlier than most disk satellites, and, not surprisingly, this results in a massive, very compact spheroidal.

$z \sim 2.2$ (red triangle in figure Fig. 3). This galaxy assembles most of its stellar mass early on, i.e., much earlier than most disk satellites. Not surprisingly, this results in a massive and very compact spheroidal system. We speculate that the very diverse stellar density and velocity dispersion properties observed in the $z \sim 2$ passive galaxy population[23] could be, at least in part, explained by a spread in the assembly epochs of its constituent galaxies.

Although the ultimate quenching of galaxies is caused by stripping of the gas reservoir and the resulting suppression of star formation after galaxies enter the group potential, we note that their star formation histories start being affected by environmental effects also prior to their infall. For most galaxies the star formation rate peaks around $z \sim 2$ at a distance of ~ 1 Mpc ($\sim$ turn-around radius) from the center of the assembling group. Afterwards, a different behavior is seen in the progenitors of the present-day population of, respectively, disk and elliptical galaxies. In the progenitors of disks, star formation declines smoothly from high to low redshift until truncation ensues, reflecting the fact that these galaxies evolve in near isolation before joining the group. On the contrary, the star formation rate of the progenitors of ellipticals, which are gas-rich, massive disk-like objects, shows high variability, with bursts caused by galaxy interactions and mergers.

As similar dichotomy occurs for gas accretion, which happens predominantly in the 'cold mode' for all galaxies prior to infall onto the group. In galaxies which remain disks down to $z = 0$, the accretion rate decreases gradually with time[24]. In the early-type galaxies, the rate is instead rather bursty and strongly modulated by the mergers these systems endure (Supplementary Information). In some galaxies, the decrease in the cold accretion rate is exacerbated by 'truncation' of the streams due to the reduction of the tidal radius of the satellites (driven by the tidal effects of the group halo potential[25]). This leads to quenching of gas accretion already at a few virial radii away from the group center. In at least one of the gas-poor disks, the supply of cold gas is already terminated when it resides in the vicinity of a $\sim 5 \times 10^{11} M_{\odot}$ halo that falls into the main group at a substantially later time.

Our work shows that the formation of $\lesssim L^*$ elliptical galaxies and 'starved' red disk galaxies in high density environments such as galaxy groups is the result of the combined effect of merging, gas removal and gas consumption processes as well as halted gas accretion naturally occurring as the potential of the group is assembled hierarchically in a ΛCDM Universe. However, elliptical galaxies are formed by mergers at high redshift prior to the formation of the final group, which is consistent with the fact that elliptical galaxies are found to be already in place at high redshift even in the field[14,26,27]. The lag of photometric transformations relative to the morphological transformations seen in our simulation indicates that many of the 'excess' blue L^* galaxies observed at $z \sim 1$, which are thought to become L^* ellipticals, but which appear to have an irregular morphology at blue rest-frame wavelengths[14,27], should show an elliptical morphology when observed at longer rest-frame wavelengths. This is a straight prediction of our simulations since at the time when their old stars acquire an elliptical morphology through mergers, the simulated galaxies still host a star forming, gaseous component. This also indicates that the tight correlation of colors and Hubble types, as well as the standard classification based on the Hubble sequence, does not hold for galaxies at redshifts higher than about 1.5-2, in good agreement with state-of-the-art studies of galaxy morphologies at such high redshifts[28]. In addition, our model predicts that the star formation and gas accretion rates of progenitors of elliptical galaxies in the considered mass range ($\sim 3 \times 10^{10} M_{\odot}$) should be highly irregular due to gas-rich galaxy interactions and mergers at intermediate redshifts $z \gtrsim 1$. Therefore, these galaxies should show a large scatter in the ages of their stellar populations and differ from single, high redshift burst models[29,30]. Future multi-wavelength

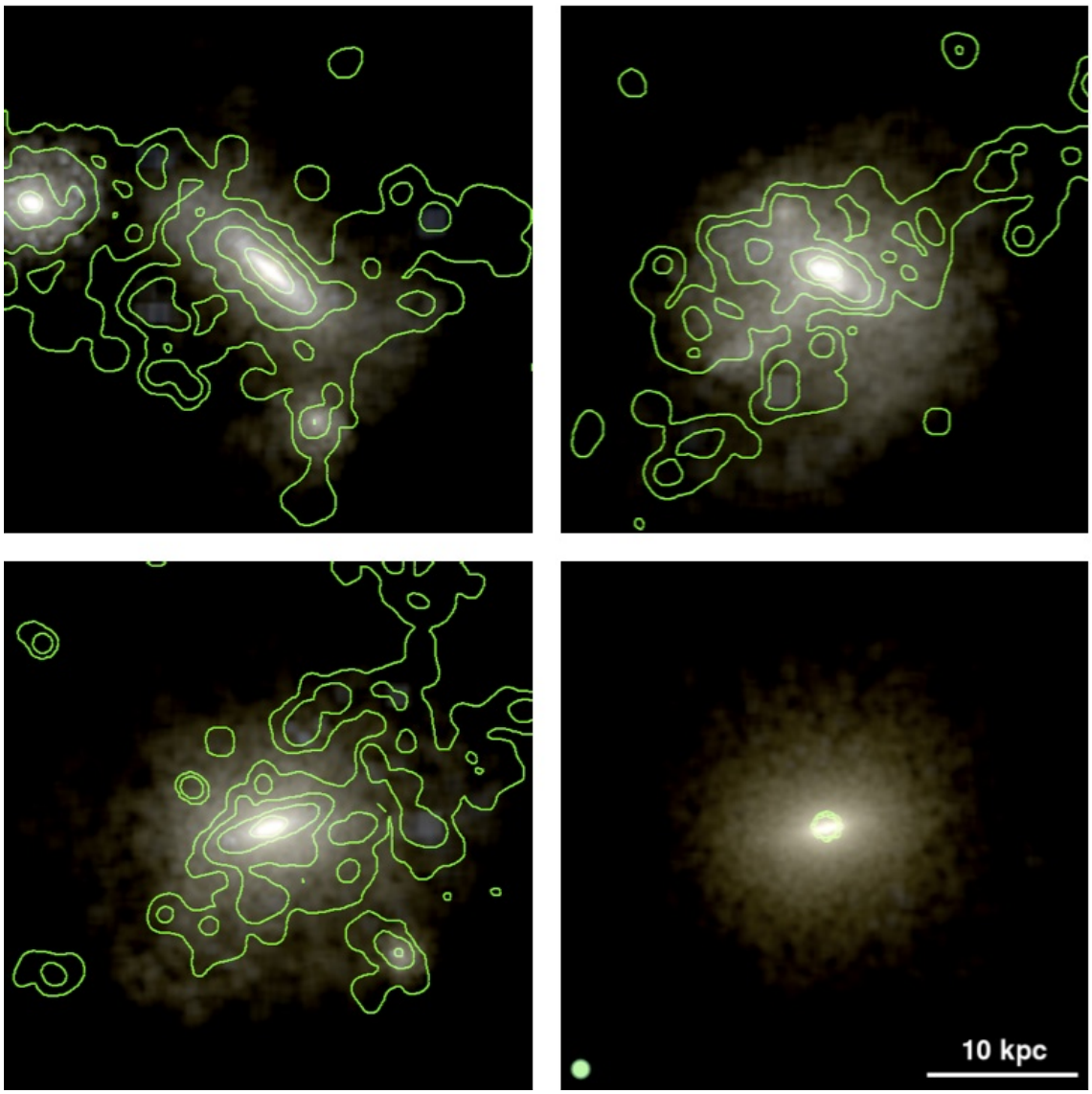

Figure 4: **Formation of a $z \sim 0$ elliptical galaxy that lives today in the relatively dense potential of a $\sim 10^{13} M_{\odot}$ galaxy group.** (Top left) Edge-on view of the $z = 1.1$ main progenitor of the elliptical galaxy # 13 in Fig. 2; the progenitor has both a stellar and a gas disk. (Top right) A gas-rich merger occurs ~ 400 Myr later, destroying the stellar disk. (Bottom left) Another 300 Myr later the stellar component of the galaxy has relaxed to an elliptical morphology, while still showing blue colors. Also, a small gas disk begins to grow again, out of the remaining cold gas. (Bottom right) At $z = 0.38$ the galaxy completes its first pericentric passage. By this time the galaxy has lost most of its cold gas, its star formation is quenched, and the colors of the galaxy are now typical of 'red sequence', passively-evolving galaxies. Column densities of neutral hydrogen are indicated by green contour lines which correspond to 0.1, 1, 10, 100 $M_{\odot}$ pc^{-2}, respectively.

observations capable of characterizing with unprecedented detail both the star formation rate evolution and the evolution of the gas content of galaxies, atomic and molecular, as a function of redshift, such as the Atacama Large Millimeter Array (ALMA), the James Webb Space Telescope (JWST) and the Square Kilometer Array (SKA), will be able to test this scenario.

Ackknowledgements R.F. acknowledges funding by the Swiss National Science Foundation. The simulations have been carried out at the Swiss National Computing Center (CSCS in Manno).

Bibliography

1. Kovac, K. et al. The 10k zCOSMOS: morphological transformation of galaxies in the group environment since z˜1. ArXiv e-prints (2009). 0909.2032.

2. Peng, Y. et al. Mass and environment as drivers of galaxy evolution in SDSS and zCOSMOS and the origin of the Schechter function. ArXiv e-prints (2010). 1003.4747.

3. Quilis, V., Moore, B. & Bower, R. Gone with the Wind: The Origin of S0 Galaxies in Clusters. Science **288**, 1617–1620 (2000). arXiv:astro-ph/0006031.

4. Cox, T. J. et al. The Kinematic Structure of Merger Remnants. *Astrophys. J.* **650**, 791–811 (2006). arXiv:astro-ph/0607446.

5. Birnboim, Y. & Dekel, A. Virial shocks in galactic haloes? *Mon. Not. R. Astron. Soc.* **345**, 349–364 (2003). arXiv:astro-ph/0302161.

6. Kawata, D. & Mulchaey, J. S. Strangulation in Galaxy Groups. *Astrophys. J., Lett.* **672**, L103–L106 (2008). 0707.3814.

7. McCarthy, I. G. et al. Ram pressure stripping the hot gaseous haloes of galaxies in groups and clusters. *Mon. Not. R. Astron. Soc.* **383**, 593–605 (2008). 0710.0964.

8. Hopkins, P. F. et al. The effects of gas on morphological transformation in mergers: implications for bulge and disc demographics. *Mon. Not. R. Astron. Soc.* **397**, 802–814 (2009). 0901.4111.

9. Springel, V., Di Matteo, T. & Hernquist, L. Modelling feedback from stars and black holes in galaxy mergers. *Mon. Not. R. Astron. Soc.* **361**, 776–794 (2005). arXiv:astro-ph/0411108.

10. Governato, F. et al. Forming disc galaxies in ΛCDM simulations. *Mon. Not. R. Astron. Soc.* **374**, 1479–1494 (2007). arXiv:astro-ph/0602351.

11. Zabludoff, A. I. & Mulchaey, J. S. The Properties of Poor Groups of Galaxies. I. Spectroscopic Survey and Results. *Astrophys. J.* **496**, 39–+ (1998). arXiv:astro-ph/9708132.

12. Balogh, M. L. & Morris, S. L. Hα photometry of Abell 2390. *Mon. Not. R. Astron. Soc.* **318**, 703–714 (2000). arXiv:astro-ph/0007111.

13. Poggianti, B. M. et al. The Star Formation Histories of Galaxies in Distant Clusters. *Astrophys. J.* **518**, 576–593 (1999). arXiv:astro-ph/9901264.

14. Bolzonella, M. et al. Tracking the impact of environment on the Galaxy Stellar Mass Function up to z˜1 in the 10k zCOSMOS sample. ArXiv e-prints (2009). 0907.0013.

15. Naab, T., Johansson, P. H., Ostriker, J. P. & Efstathiou, G. Formation of Early-Type Galaxies from Cosmological Initial Conditions. *Astrophys. J.* **658**, 710–720 (2007). arXiv:astro-ph/0512235.

16. Wadsley, J. W., Stadel, J. & Quinn, T. Gasoline: a flexible, parallel implementation of TreeSPH. New Astronomy **9**, 137–158 (2004). arXiv:astro-ph/0303521.

17. Brooks, A. M., Governato, F., Quinn, T., Brook, C. B. & Wadsley, J. The Role of Cold Flows in the Assembly of Galaxy Disks. *Astrophys. J.* **694**, 396–410 (2009). 0812.0007.

18. Stinson, G. et al. Star formation and feedback in smoothed particle hydrodynamic simulations - I. Isolated galaxies. *Mon. Not. R. Astron. Soc.* **373**, 1074–1090 (2006). arXiv:astro-ph/0602350.

19. Feldmann, R. et al. The Evolution of Central Group Galaxies in Hydrodynamical Simulations. *Astrophys. J.* **709**, 218–240 (2010). 0906.3022.

20. Larson, R. B., Tinsley, B. M. & Caldwell, C. N. The evolution of disk galaxies and the origin of S0 galaxies. *Astrophys. J.* **237**, 692–707 (1980).

21. Mihos, J. C. & Hernquist, L. Gasdynamics and Starbursts in Major Mergers. *Astrophys. J.* **464**, 641–+ (1996). arXiv:astro-ph/9512099.

22. Blanton, M. R. et al. The Galaxy Luminosity Function and Luminosity Density at Redshift z = 0.1. *Astrophys. J.* **592**, 819–838 (2003). arXiv:astro-ph/0210215.

23. van Dokkum, P. G., Kriek, M. & Franx, M. A high stellar velocity dispersion for a compact massive galaxy at redshift z = 2.186. *Nature* **460**, 717–719 (2009). 0906.2778.

24. Sommer-Larsen, J., Götz, M. & Portinari, L. Galaxy Formation: Cold Dark Matter, Feedback, and the Hubble Sequence. *Astrophys. J.* **596**, 47–66 (2003). arXiv:astro-ph/0204366.

25. Hahn, O., Porciani, C., Dekel, A. & Carollo, C. M. Tidal effects and the environment dependence of halo assembly. *Mon. Not. R. Astron. Soc.* **398**, 1742–1756 (2009). 0803.4211.

26. Cimatti, A., Daddi, E. & Renzini, A. Mass downsizing and "top-down" assembly of early-type galaxies. *Astron. Astrophys.* **453**, L29–L33 (2006). arXiv:astro-ph/0605353.

27. Scarlata, C. et al. The Redshift Evolution of Early-Type Galaxies in COSMOS: Do Massive Early-Type Galaxies Form by Dry Mergers? *Astrophys. J., Suppl. Ser.* **172**, 494–510 (2007). arXiv:astro-ph/0701746.

28. Cameron, E. et al. Color-selection criteria and rest-frame optical morphologies of 1.5 ¡ z ¡ 3.5 active and passive galaxies with WFC3. ArXiv e-prints (2010). 1007.2422.

29. Gallazzi, A., Charlot, S., Brinchmann, J., White, S. D. M. & Tremonti, C. A. The ages and metallicities of galaxies in the local universe. *Mon. Not. R. Astron. Soc.* **362**, 41–58 (2005). arXiv:astro-ph/0506539.

30. Thomas, D., Maraston, C., Bender, R. & Mendes de Oliveira, C. The Epochs of Early-Type Galaxy Formation as a Function of Environment. *Astrophys. J.* **621**, 673–694 (2005). arXiv:astro-ph/0410209.

31. Spergel, D. N. et al. Three-Year Wilkinson Microwave Anisotropy Probe (WMAP) Observations: Implications for Cosmology. *Astrophys. J., Suppl. Ser.* **170**, 377–408 (2007). arXiv:astro-ph/0603449.

32. Bertschinger, E. Multiscale Gaussian Random Fields and Their Application to Cosmological Simulations. *Astrophys. J., Suppl. Ser.* **137**, 1–20 (2001). arXiv:astro-ph/0103301.

33. Gill, S. P. D., Knebe, A. & Gibson, B. K. The evolution of substructure - I. A new identification method. *Mon. Not. R. Astron. Soc.* **351**, 399–409 (2004). arXiv:astro-ph/0404258.

34. Knollmann, S. R. & Knebe, A. AHF: Amiga's Halo Finder. *Astrophys. J., Suppl. Ser.* **182**, 608–624 (2009). 0904.3662.

35. Carollo, C. M., Danziger, I. J. & Buson, L. Metallicity Gradients in Early Type Galaxies. *Mon. Not. R. Astron. Soc.* **265**, 553–+ (1993).

36. Treu, T., Stiavelli, M., Møller, P., Casertano, S. & Bertin, G. The properties of field elliptical galaxies at intermediate redshift - II. Photometry and spectroscopy of an HST-selected sample. *Mon. Not. R. Astron. Soc.* **326**, 221–236 (2001). arXiv:astro-ph/0104177.

37. Bruzual, G. & Charlot, S. Stellar population synthesis at the resolution of 2003. *Mon. Not. R. Astron. Soc.* **344**, 1000–1028 (2003). arXiv:astro-ph/0309134.

38. Maraston, C. Evolutionary population synthesis: models, analysis of the ingredients and application to high-z galaxies. *Mon. Not. R. Astron. Soc.* **362**, 799–825 (2005). arXiv:astro-ph/0410207.

39. Charlot, S. & Fall, S. M. A Simple Model for the Absorption of Starlight by Dust in Galaxies. *Astrophys. J.* **539**, 718–731 (2000). arXiv:astro-ph/0003128.

40. Kereš, D., Katz, N., Weinberg, D. H. & Davé, R. How do galaxies get their gas? *Mon. Not. R. Astron. Soc.* **363**, 2–28 (2005). arXiv:astro-ph/0407095.

41. Kereš, D., Katz, N., Fardal, M., Davé, R. & Weinberg, D. H. Galaxies in a simulated ΛCDM Universe - I. Cold mode and hot cores. *Mon. Not. R. Astron. Soc.* **395**, 160–179 (2009). 0809.1430.

42. Peng, C. Y., Ho, L. C., Impey, C. D. & Rix, H.-W. Detailed Structural Decomposition of Galaxy Images. *Astron. J.* **124**, 266–293 (2002). arXiv:astro-ph/0204182.

43. Mayer, L., Governato, F. & Kaufmann, T. The formation of disk galaxies in computer simulations. Advanced Science Letters **1**, 7–27 (2008). 0801.3845.

44. Dressler, A. et al. Spectroscopy and photometry of elliptical galaxies. I - A new distance estimator. *Astrophys. J.* **313**, 42–58 (1987).

45. Bender, R., Burstein, D. & Faber, S. M. Dynamically hot galaxies. I - Structural properties. *Astrophys. J.* **399**, 462–477 (1992).

46. Tully, R. B. & Fisher, J. R. A new method of determining distances to galaxies. *Astron. Astrophys.* **54**, 661–673 (1977).

47. Meza, A., Navarro, J. F., Steinmetz, M. & Eke, V. R. Simulations of Galaxy Formation in a ΛCDM Universe. III. The Dissipative Formation of an Elliptical Galaxy. *Astrophys. J.* **590**, 619–635 (2003). arXiv:astro-ph/0301224.

48. Graves, G. J., Faber, S. M. & Schiavon, R. P. Dissecting the Red Sequence. II. Star Formation Histories of Early-Type Galaxies Throughout the Fundamental Plane. *Astrophys. J.* **698**, 1590–1608 (2009). 0903.3603.

49. Verheijen, M. A. W. & Sancisi, R. The Ursa Major cluster of galaxies. IV. HI synthesis observations. *Astron. Astrophys.* **370**, 765–867 (2001). arXiv:astro-ph/0101404.

50. Verheijen, M. A. W. The Ursa Major Cluster of Galaxies. V. H I Rotation Curve Shapes and the Tully-Fisher Relations. *Astrophys. J.* **563**, 694–715 (2001). arXiv:astro-ph/0108225.

51. Bell, E. F. & de Jong, R. S. Stellar Mass-to-Light Ratios and the Tully-Fisher Relation. *Astrophys. J.* **550**, 212–229 (2001). arXiv:astro-ph/0011493.

Supplementary Information

A Simulation details

The simulation set-up and the employed zoom-in technique is described in detail elsewhere[19]. In brief, a group halo is selected from a dark matter simulation of a 123 Mpc periodic box. Higher resolution initial conditions centered on the group with WMAP-3 cosmological parameters[31] are generated using `grafic-2`[32]. The simulation is run with the parallel TreeSPH code `GASOLINE`[16]. The mass (force) resolution of the simulation is $6.4 \times 10^6\ M_\odot$ (0.5 kpc), $1.4 \times 10^6\ M_\odot$ (0.3 kpc) and $4 \times 10^5\ M_\odot$ (0.3 kpc) for dark matter, SPH and star particles, respectively.

B Halo extraction and the measurement of their properties

Halos and halo centers are identified with the AMIGA HaloFinder[33,34] (AHF), that is capable of detecting subhalos (our satellites) within halos (our group). Halos extend out to the virial radius R_{200}, which we define as the radius enclosing a mean matter density of $200/\Omega_m$ times the mean density of the universe, or out to the tidal radius, whichever is smaller. We then use the following technique to track satellites over time. First, we identify each halo h in each snapshot s below $z = 4$ that (a) has a bound mass of more than $1.4 \times 10^{10}\ M_\odot$, (b) contains more than 50000 particles, and (c) lies within 630 comoving kpc from the group center. Second, for each such determined halo h_s we determine its main progenitor h_{s-1} in the previous snapshot and its main successor h_{s+1} in the following snapshot and construct a complete timeline $(h_0, \ldots, h_s, \ldots, h_n)$ by recursion. Let N_1, N_2 and $N_{\rm common}$ be the number of particles in halo h_1, the number of particles in halo h_2 and the number of particles common to both halos, respectivley. Then the ratio $\eta(h_1, h_2)$, defined as $\eta(h_1, h_2) = N_{\rm common}^2/(N_1 N_2)$, can be used to define main successors and progenitors. We define the halo from snapshot $s + 1$ with the largest η (any halo is in principle eligible, not only the ones selected as described above) as main successor of halo h_s. The main progenitor is found in the same way except that the parent group halo is excluded as progenitor. Since the group halo h_G (and its associated central galaxy) are allowed as main progenitor this algorithm often finds multiple timelines for a given halo h_s. For example the following timelines of halo h_s could be produced $(h_0, \ldots, h_s, h_{s+1}, \ldots, h_n)$, $(h_0, \ldots, h_s, h_{s+1}, h_G, \ldots, h_G)$, $(h_0, \ldots, h_s, h_G \ldots, h_G)$. In this case we only keep the timeline that traces the halo h_s as long as possible as an entity separate from the group halo (which is the first timeline in the example). Following this procedure we obtain ~ 20 satellites of which 13 have not merged with the central galaxy by $z \sim 0.1$.

Unless noted otherwise star formation rates (SFR) are measured within a sphere of 20 physical kpc. The specific star formation rate is obtained by dividing the SFR by the stellar mass. Stellar masses are defined as the mass of the stellar component that is bound to the halo (using AHF) within a sphere of 20 physical kpc. Kinematical properties are determined by putting a slit that is 24 kpc long, 4 kpc wide and contains 24 bins along the 2D major axis of an edge-on view of the galaxy. The rotation velocities and dispersions are then determined from the moments of the line-of-sight velocities. Maximal rotation velocities $v_{\rm rot}$ are taken to be half the difference between the maximum and the minimum rotation velocity. Central velocity dispersions $\sigma_{\rm cen}$ are measured within a 1 kpc aperture, but excluding the central softening length. The measured value is increased by a factor 1.1 to account for the radial decline of the velocity dispersion[35,36]. Cold gas is defined as the gas with a temperature of less then 3.2×10^4 K, unless noted otherwise. The neutral hydrogen mass is derived

from the hydrogen mass fraction that is calculated within GASOLINE during the simulation. Our simulation does not include an explicit treatment of molecular hydrogen. Hence, in the analysis we do distinguish between atomic and molecular hydrogen components. Colors (all in the AB-system) are derived from stellar synthesis models, typically from the models of [37], but we have also tested the single stellar populations of [38] finding that the latter reddens the $B-I$ color at $z\sim 0$ of galaxies with $B-I\lesssim 1.1$ by up to 0.1 mag. Hence uncertainties in the stellar population models are unlikely to have strong effects on our results, but can nonetheless change colors and magnitudes by a few percent.

We reduce the effect of star formation in the central region on the colors by fixing the mass-to-light ratio within one softening length to its value at one softening length. In order to estimate the effect of a very young (<100 Myr) stellar component we have tested a simplified version of the dust-obscuration model of [39], namely reducing the flux of the very young stellar particles to zero as done in, e.g. [15], but not applying any further dust corrections. We find that galaxies with $B-I$ colors below ~ 1 are typically reddened by $0.05-0.1$ mag and redder galaxies are affected on a less than 0.05 mag level. Given that the corrections are overall rather small we will refer to the single stellar populations of [37] without a flux reduction of very young stars.

The SPH technique allows us to follow the temperature history of individual gas parcels (SPH particles). In order to assess whether accreted gas has been cooled from a hot halo or whether it stayed cold since the beginning of the simulation we assign each gas particle the maximum temperature in its history. We do not update the maximum temperature if the gas particle is less than 30 kpc away from the satellite center in order to avoid that its maximum temperature is set by supernova feedback, see [17]. We use a temperature threshold of 2.5×10^5 K to separate hot and cold accretion[40,41], which despite its simplicity gives similar results compared to more sophisticated treatments[17]. Star particles inherit the maximum temperature from their parent gas particles. To obtain instantaneous gas and stellar accretion rates onto a satellite galaxy we first determine its center-of-mass velocity from all particles within a sphere of 20 kpc. Radial velocities v^r of gas and star particles are then computed in the rest-frame of the satellite. We estimate the mass flux through a spherical shell at $r=35$ kpc distance from the center by summing over all contained particles:

$$dM/dt \approx 4\pi r^2 \rho \sum_i m_i v_i^r / \sum_i m_i = 4\pi r^2 \sum_i m_i v_i^r / V.$$

Here, ρ and V are the mean density and volume of the spherical shell. Its thickness is 10 kpc to ensure that it contains at least several hundred gas particles. For the accretion of bound material we only include the particles identified as bound to the satellite by AHF, otherwise we use all the particles in the shell.

We quantify the mass loss of cold gas due to consumption and stripping by tracing forward in time the cold gas particles that are contained within 20 kpc at a snapshot $\sim 100-200$ Myr before infall time. We consider that an initially cold gas particle may be kept as gas particle within a 20 kpc distance ("kept"), that it may be kept after the transformation into a star particle ("consumed"), or that it is leaves the 20 kpc radius ("stripped"). A small, but non-negligible fraction of the "kept" gas is heated, e.g. by supernova feedback. However, to first order the heating and cooling of gas should balance and hence the heated gas mass will be replaced by a similar gas mass of cooled gas. Hence, the "kept" gas mass should roughly correspond to the kept cold gas mass. The stated mass fractions and errors refer to the mean and the standard deviation of the various mass fractions for all $z\sim 0.1$ gas-poor satellites.

We measure single component Sersic indices $n_{\rm sersic}$ on face-on and edge-on 2D mock images with

GALFIT[42]. In particular, we compute noise ("sigma") maps based on the particle-per-pixel number in mock images of the surface mass density assuming a Poisson statistics. We exclude the central 3 softening lengths from the fit and use the average value of the face-on and edge-on $n_{\rm sersic}$ value. This approach substantially reduces the spurious effects of 'overcooling'[43] in the morphological classification, as it puts weight on the mass profile outside the very central regions. Our classification criterion, albeit coarse, allows us nonetheless to distinguish between the disk and elliptical satellites which are discussed in the main text.

C Scaling relations for the simulated satellite galaxies

Real galaxy populations are observed to obey fundamental scaling laws, such as the fundamental plane (FP) relation[44,45] and the Tully-Fisher relation[46]. The FP for elliptical galaxies shows that most such galaxies populate a thin two-dimensional surface in the three-dimensional space of characteristic stellar velocity σ, half-light radius $r_{\rm eff}$ and surface brightness within the half-light radius, $\Sigma_{\rm eff}$. The FP reflects the virial relation between masses, sizes and velocities; the observed tilt relative to the virial plane is interpreted with a dependence of the mass-to-light ratio with galaxy mass. Similarly, the TF relation connects the luminosity of disk galaxies and their rotation velocities. Observations indicate $L \propto V_{\rm rot}^{\alpha}$ with $\alpha = 3 - 4$ depending on wavelength and how dust extinction is modeled.

We use these scaling laws to assess how similar, in their global properties, our simulated objects are to real galaxies. For this purpose we extract from the last simulation snapshot ($z \sim 0.1$) the following properties for the satellites: (1) B-band circular effective radii $r_{\rm eff}$, that include half the total B-band flux within projected 20 kpc. The flux from within one baryonic softening length is derived from the included mass and the mass-to-light ratio at one softening length. (2) The B-band surface brightness which is proportional to the B-band flux divided by $r_{\rm eff}^2$. (3) The stellar B-band line-of sight velocity dispersion and rotation velocity. (4) The line-of-sight rotation velocity of neutral hydrogen for the two disk satellites with a sufficient cold gas content at $z \sim 0.1$, measured as for the stellar component.

In the left panel of Fig. 14 we analyze the position of the simulated galaxies within the FP. Four of the seven early-type galaxies in our simulated sample have FP properties of real galaxies of similar type. The remaining three are slightly more compact. Numerical effects or missing physical ingredients are likely to play a role in generating this effect[19,47]. We also expect a small shift between simulated and real galaxies on any such diagram on merely technical grounds. In particular, the practical decision of truncating the light of the simulated galaxies at 20 kpc will bias their half-light radius towards smaller values. Furthermore, in the right panel of Fig. 14 we show that the disk galaxies among the simulated satellites follow reasonably well the observed TF relation, and particularly when the rotation velocity derived for neutral hydrogen is used for the comparison. We conclude that, overall, the simulated galaxies match the fundamental scaling laws obeyed by the $\lesssim L^*$ $z = 0$ galaxy population reasonably well.

Of course, the match between real and simulated galaxies is neither expected nor observed to be yet perfect. Still, we have come a long way in reproducing the rich diversity of the $z = 0$ galaxy population, from disks to ellipticals. This is achieved with numerical recipes for star formation and stellar feedback which were originally tuned to produce a Milky-Way-type galaxy[10,18]. Thus, along with achieving a higher level of sophistication, and enabling a deeper understanding of the spurious numerical effects, the current generation of

cosmological hydrodynamical simulations is also genuinely paving the road to a clearer understanding of the physical processes which lead to the full complexity of the Hubble sequence.

D Supplementary Tables

Satellite Classification	$z = 0.1$	$z = 0.5$	$z = 1$	$z = 2$
# red	9	4	0	0
# blue	4	9	13	13
# gas-poor	10 (9)	5 (2)	1 (1)	0 (0)
# intermediate-gas	3 (3)	8 (6)	9 (3)	2 (1)
# gas-rich	0 (1)	0 (5)	4 (9)	11 (12)
# quiescent	9	4	1	0
# star forming	4	7	6	1
# strongly SF	0	2	6	12
# quiescent (total)	8	1	0	0
# star forming (total)	4	8	4	0
# strongly SF (total)	1	4	9	13

Table 1: The classification of $z \sim 0.1$ group satellites with stellar masses above 10^{10} $M_{\odot}$ and their main progenitors. The rest frame $B - I$ color is used to define red ($B - I \geq 1$) and blue ($B - I < 1$) galaxies. Galaxies are defined as gas-rich if they have a HI-to-stellar mass ratio or (for the values given in brackets) a cold gas-to-stellar mass ratio in excess of 10%. Gas-poor galaxies have $f_{\rm gas}$ <1%. Galaxies with $f_{\rm gas}$ in the range 1-10% are referred to as intermediate-gas systems. Galaxies with specific SFRs (SSFRs) < 0.02 Gyr^{-1} are defined as quiescent galaxies, and otherwise as star forming galaxies. Galaxies are furthermore considered to be 'strongly star forming' if their SSFR is larger than the inverse of the age of the Universe, i.e. SSFR $>$ 0.08 Gyr^{-1} at $z = 0.1$. The classification in the last three rows differs from the one in the previous three rows due to the inclusion of the star formation occurring within the unresolved central softening length $\epsilon_{\rm bar}$. Note that at $z \sim 1 - 2$ most progenitors are blue, gas rich, star forming galaxies.

E Supplementary Figures

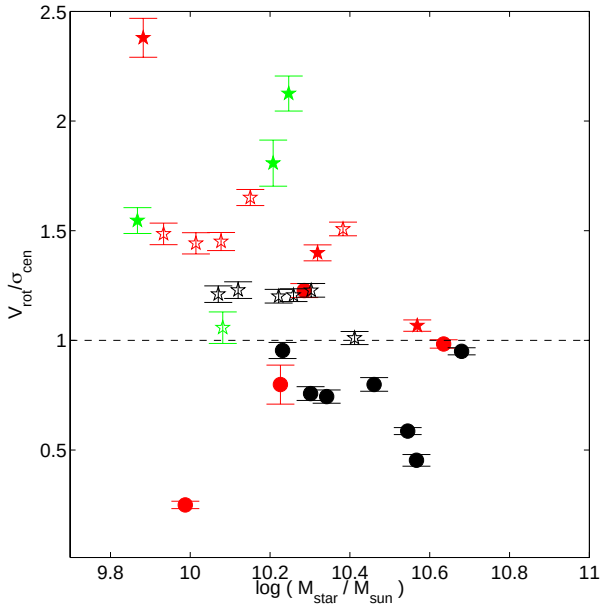

Figure 5: The kinematic properties of massive $z = 0$ satellites and their progenitors. Shown is the ratio of maximum stellar line-of-sight rotation velocity and central velocity dispersion vs. stellar mass $M_{\rm star}(z)$. Plotted are the 13 satellites with mass in excess of $10^{10} M_\odot$ at $z = 0.1$. The redshift z is indicated by color: $z = 0.1$ (black), $z = 1$ (red), $z = 2$ (green); Circles (stars) indicate galaxies with a spericity larger (smaller) than 0.45; filled (empty) symbols denote galaxies that are classified at $z = 0.1$ as elliptical (disk) galaxies. At $z \sim 1 - 2$ most progenitors are rotation-supported galaxies.

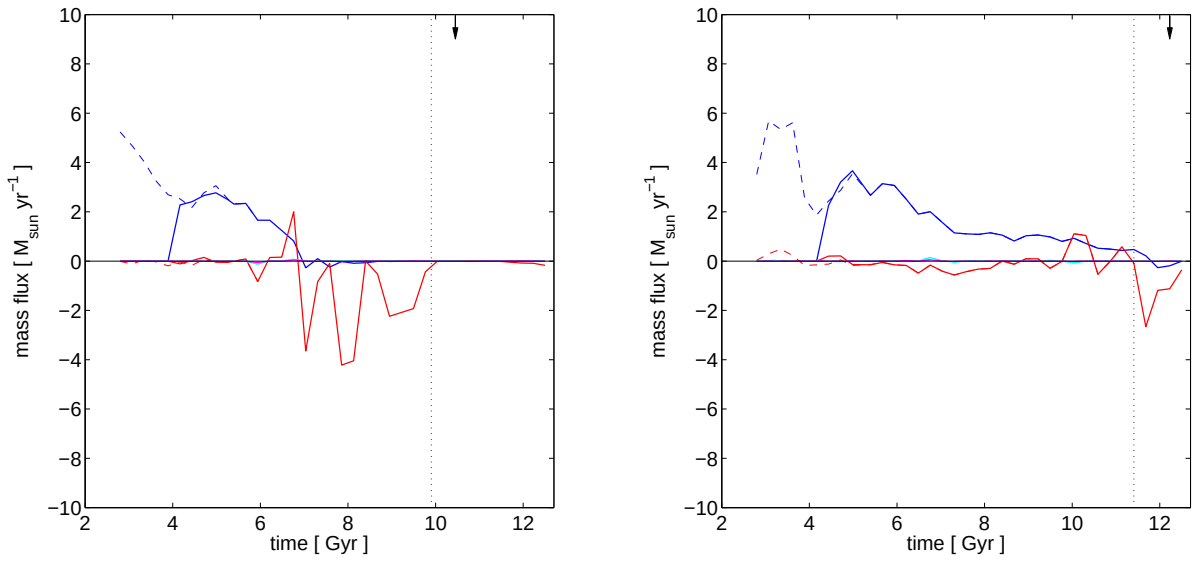

Figure 6: The gas accretion history of *(left)* a $z = 0$ gas-poor disk satellite (#3 in Fig. 2) and *(right)* a $z = 0$ intermediate-gas disk satellite (#2 in Fig. 2). Shown are the instantaneous accretion rates of gas that was never heated above $T_{\rm thres} = 2.5 \times 10^5$ K (cold accretion, blue line), and of gas heated above that threshold (hot accretion, red line). The dotted vertical line denotes the infall time into the group, arrows indicate pericentric passages. The solid line includes only particles bound to the satellite, while the dashed line includes all particles (only shown before infall). Contrary to the accretion histories of elliptical satellite progenitors (e.g. Fig. 7) the gas accretion of disk satellite progenitors proceeds in a smooth fashion. The gas accretion of the gas-poor disk is already quenched at $t \sim 7$ Gyr, when it resides in a small neighboring group. The gas accretion of the intermediate-gas disk is terminated after infall to the main group. Just before the infall the density of the hot gas increases as the satellite enters the group halo, which is filled with hot, shock-heated intragroup gas. Shortly afterwards, ram pressure stripping removes a large fraction of the satellite's own hot halo gas[7].

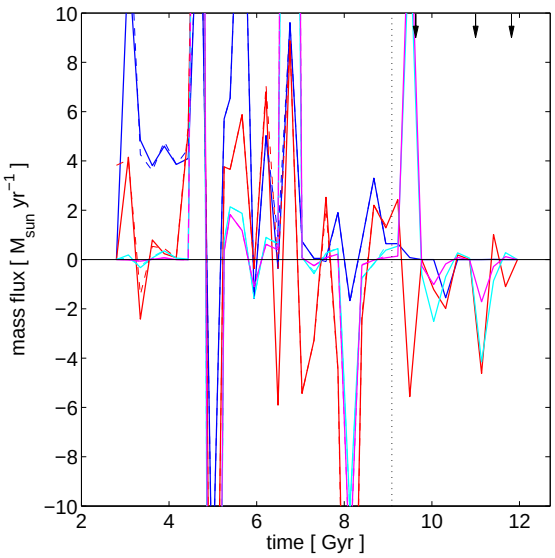

Figure 7: The gas accretion history of a $z = 0$ elliptical satellite (#13 in Fig. 2) is very irregular. Symbols are as in Fig. 6. The accretion of stellar particles that are formed by gas particles heated (cyan) or not heated (magenta) above $T_{\rm thres}$ is also shown. Cold accretion dominates at early times ($t < 4$ Gyr). At later times, but before the fall into the group, the gas accretion history is dominated by mergers. At the latest epochs the group environment quenches any further gas accretion onto the satellite.

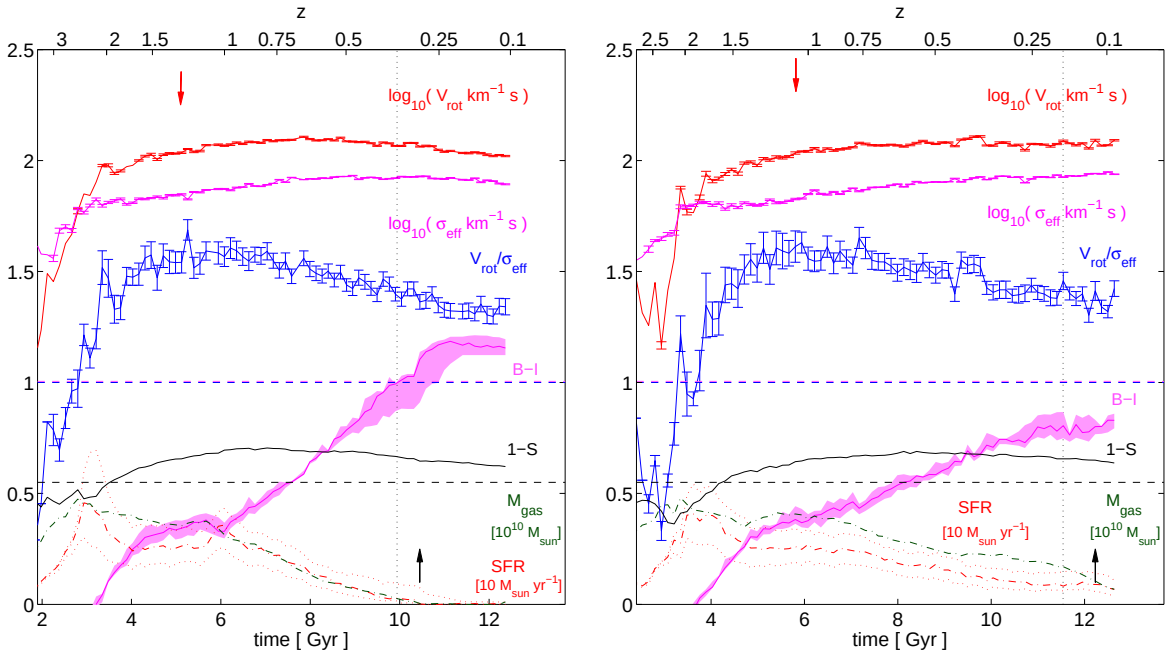

Figure 8: The evolution of (left) a $z \sim 0$ gas-poor disk satellite (#3 in Fig. 2) and (right) a $z \sim 0$ intermediate-gas disk satellite (#2 in Fig. 2). Shown are the line of sight velocity dispersion (magenta line with errorbars), the maximum of the line-of-sight rotation velocity (red line with errorbars), v/σ (blue line with errorbars), the non-sphericity 1- c/a (black solid line), the amount of cold gas ($< 3.2 \times 10^4$ K) within 20 kpc (green dot-dashed line), the star formation rate within 10 kpc (upper red dotted line), within 10 kpc excluding 1 softening length (red dot-dashed line), within 10 kpc excluding 2 softening length (lower red dotted line), the $B - I$ color (magenta shaded area; the upper and lower limits are measured within 10 kpc excluding and including the central 2 softening lengths, while the magenta line is measured by excluding the central softening length). The red arrow at the top left is the time when half of the stellar mass is formed. The vertical dotted line denotes the time of infall into the group and the black arrows on the bottom right denote pericentric passages.

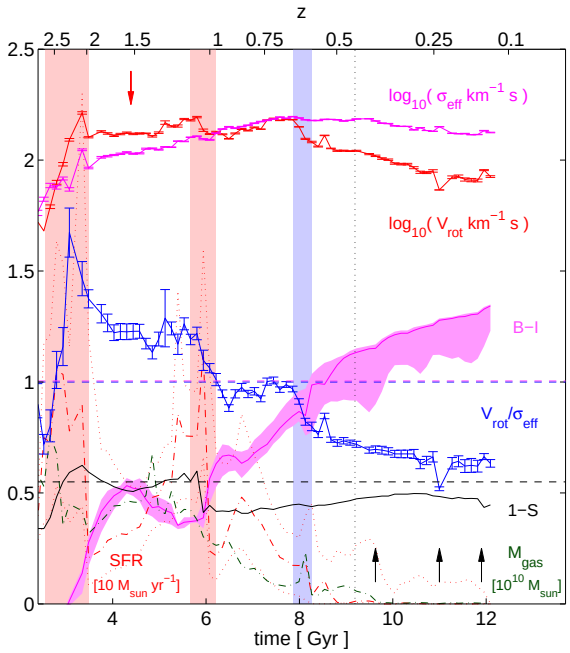

Figure 9: The evolution of a $z \sim 0$ elliptical satellite (#13 in Fig. 2). Symbols are as in Fig. 8. The vertical shaded areas denote prominent mergers (red) or a fly-by (blue).

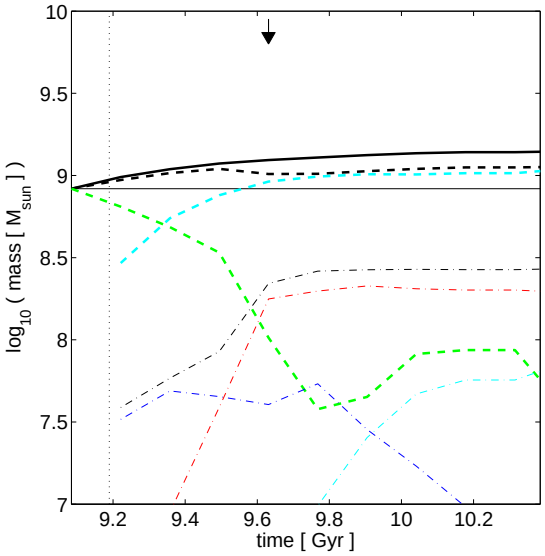

Figure 10: The fate of the cold gas in a $z \sim 0$ elliptical satellite (#13 in Fig. 2). The cold gas particles contained within a sphere of 20 kpc radius around the satellite are identified in a snapshot before infall time (vertical dotted line) and traced forward in time. The solid black line shows the total mass of all successor particles of the selected cold gas particles. This mass is not conserved but slightly increases due to stellar winds from the satellite's own stellar population. The mass that remains within (< 20 kpc) the satellite is shown as dashed black line, while the mass of stripped (> 20 kpc) particles is shown with a dot-dashed black line. The other lines correspond to the amount of gas that remains and stays cold (dashed green line), that is transformed into stars that remain within the satellite (dashed cyan line), that is stripped (dot-dashed black line), is stripped and heated (dot-dashed red line), is stripped and stays cold (dot-dashed blue line) or is transformed into stripped stars (dot-dashed cyan line). About 75% of the cold gas reservoir present before infall to the group is quickly converted into stars, while $\sim 20\%$ is stripped between infall time and the first pericentric passage (vertical arrow).

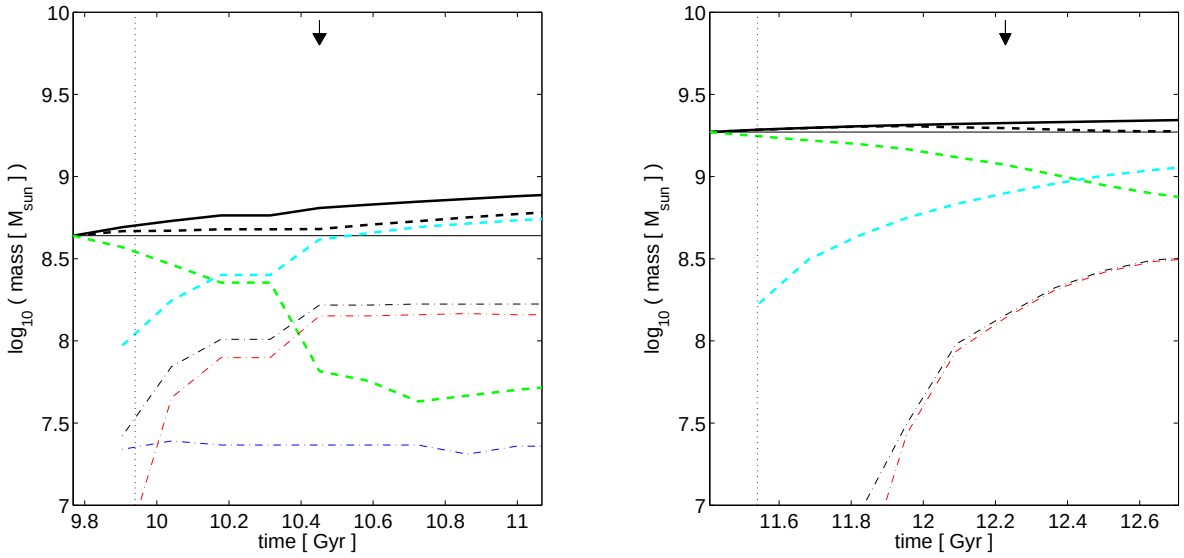

Figure 11: The fate of the cold gas in (left) a $z \sim 0$ gas-poor disk satellite (#3 in Fig. 2) and (right) a $z \sim 0$ intermediate-gas disk satellite (#2 in Fig. 2). Symbols are as in Fig. 10.

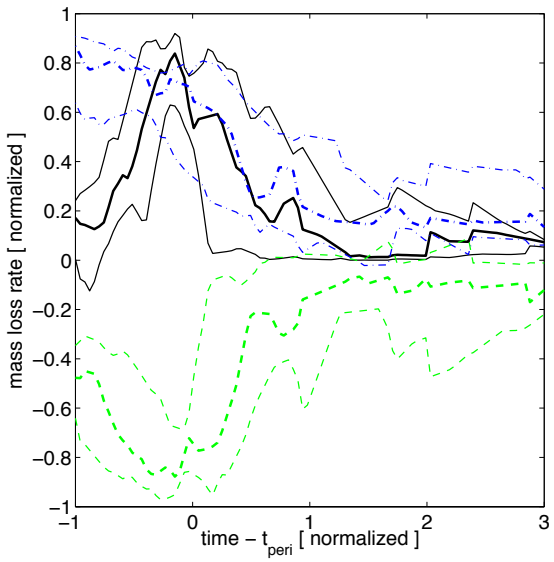

Figure 12: The effects of pericenter passages in the evolution of the satellites. The figure shows the average cold gas transformation rates obtained after stacking all satellites together on normalized axes. The time axis is normalized in units of $t_{\rm peri} - t_{\rm infall}$, while the rates of each individual satellite are normalized to its maximum value. Thick (thin) lines denote the median (lower/upper quartile) of the satellite population. Most of the cold gas that resides in satellites just before they infall into the group (green dashed lines; shown with the negative of the mass loss rate for better visualization) is either continuously transformed into stars (blue dotted lines) or stripped (black solid lines) in pericentric passages. Some satellites show enhanced star formation rates close to pericenter time. However, overall, the conversion of cold gas into stars is strongly reduced after the first pericentric passage. Within a time scale of about $t_{\rm peri} - t_{\rm infall}$ after pericenter passage, the cold gas reservoir is exhausted and the mass loss rates become negligible.

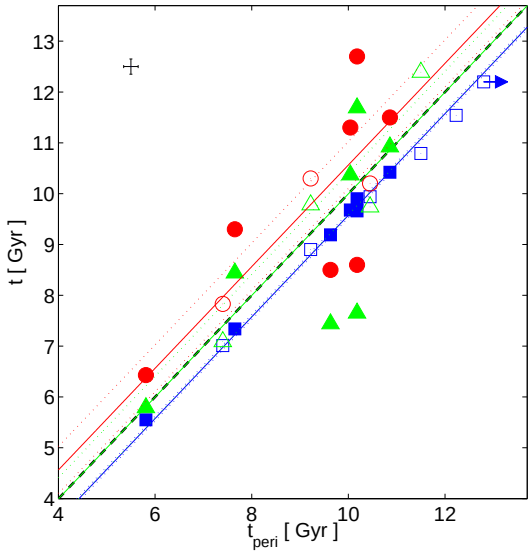

Figure 13: Time of first pericentric passage of a $z \sim 0$ elliptical (filled symbols) and disk (empty symbols) satellite vs infall time into the group (blue squares). Also shown are the time at which the HI-to-stellar-mass ratio $f_{\rm gas}$ finally drops below 1% (green triangles), and the time at which $B - I > 1$ (red circles). Linear fits with unity slope are shown as colored solid lines, the fit errors as dotted lines. The satellites approach their first pericentric passage typically 0.4 ± 0.1 Gyr after infall into the group and, by then, turn into gas-poor ($f_{\rm gas} < 1\%$) galaxies. On average 0.6 ± 0.5 Gyr later the galaxies become red. The error of a typical data point that arises from the limited time resolution of the simulation is indicated at the top left. The arrow at the top right highlights a gas-rich disk that has not yet completed its first pericentric passage. A Spearman rank test shows a correlation, at the level of 2.8σ and 2.2σ, respectively, between pericentric time and both the time when $f_{\rm gas}$ drops below 1%, and the time when the galaxy turns red.

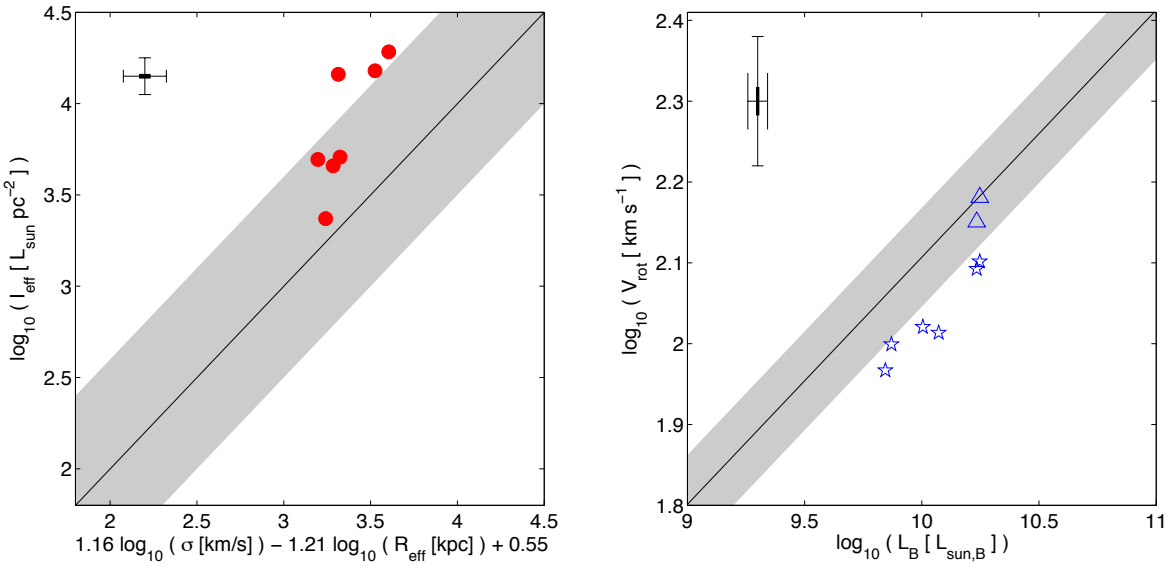

Figure 14: Comparison between simulated and observed galaxy scaling relations. Simulated values are inferred from the $z \sim 0.1$ snapshot; blue (empty) and red (filled) symbols correspond to satellites that are classified as disks and ellipticals, respectively. *Left:* Projection of the fundamental plane of early-type galaxies adopted from [48]. The gray stripe indicates the location of real galaxies and red dots are our simulated objects with an early type morphology by redshift $z \sim 0.1$. *Right:* The Tully fisher relation. Circles show B-band luminosities and maximum stellar (B-band flux-weighted) line-of-sight rotation velocities of the disk satellites; triangles show maximum line-of-sight rotation velocities of neutral hydrogen for the two disk satellites with $f_{\rm gas} > 3\%$. The solid line shows the mass dependent dust-corrected B-band Tully Fisher relation derived from the rotation velocities of neutral hydrogen of spiral galaxies in the Ursa Major cluster[49–51] and the shaded area indicates its typical scatter of 0.5 mag. Error bars in the top left corners of each figure include statistical errors for individual satellites (including Poisson noise in the galaxy representations, binning errors and fitting errors), and an estimate of the systematic errors in converting simulated data into observables. These systematic errors include contributions from the fixed aperture measurements used to measure the half-light radii, from estimating the luminosities from stellar synthesis models, from neglecting dust effects, as well as from differences between kinematic data extracted from moments and from Gauss-Hermitian fits.